Crystal Structure and Amide H/D Exchange of Binary Complexes of Alcohol Dehydrogenase from *Bacillus stearothermophilus*: Insight into Thermostability and Cofactor Binding[†,‡]

Christopher Ceccarelli,[§] Zhao-Xun Liang,[||] Michael Strickler,[⊥,#] Gerd Prehna,[⊥,£] Barry M. Goldstein,[⊥] Judith P. Klinman,[||] and Brian J. Bahnson*[,§]

Department of Chemistry and Biochemistry, University of Delaware, Newark, Delaware 19716, Department of Chemistry, University of California at Berkeley, Berkeley, California 94720, and Department of Biophysics, University of Rochester, Rochester, New York 14627

Received February 5, 2004; Revised Manuscript Received March 9, 2004

ABSTRACT: The crystal structure of NAD^+-dependent alcohol dehydrogenase from *Bacillus stearothermophilus* strain LLD-R (htADH) was determined using X-ray diffraction data at a resolution of 2.35 Å. The structure of homotetrameric htADH is highly homologous to those of bacterial and archaeal homotetrameric alcohol dehydrogenases (ADHs) and also to the mammalian dimeric ADHs. There is one catalytic zinc atom and one structural zinc atom per enzyme subunit. The enzyme was crystallized as a binary complex lacking the nicotinamide adenine dinucleotide (NAD^+) cofactor but including a zinc-coordinated substrate analogue trifluoroethanol. The binary complex structure is in an open conformation similar to ADH structures without the bound cofactor. Features important for the thermostability of htADH are suggested by a comparison with a homologous mesophilic enzyme (55% identity), NAD^+-dependent alcohol dehydrogenase from *Escherichia coli*. To gain insight into the conformational change triggered by NAD^+ binding, amide hydrogen−deuterium exchange of htADH, in the presence and absence of NAD^+, was studied by HPLC-coupled electrospray mass spectrometry. When the deuteron incorporation of the protein-derived peptides was analyzed, it was found that 9 of 21 peptides show some decrease in the level of deuteron incorporation upon NAD^+ binding, and another 4 peptides display slower exchange rates. With one exception (peptide number 8), none of the peptides that are altered by bound NAD^+ are in contact with the alcohol−substrate-binding pocket. Furthermore, peptides 5 and 8, which are located outside the NAD^+-binding pocket, are notable by displaying changes upon NAD^+ binding. This suggests that the transition from the open to the closed conformation caused by cofactor binding has some long-range effects on the protein structure and dynamics.

NAD^+-dependent alcohol dehydrogenase (ADH,[1] EC 1.1.1.1) catalyzes the reversible oxidation of a wide range of aliphatic and aromatic alcohols to their corresponding aldehydes or ketones using NAD^+ as the cofactor (*1*). ADH is found in many different organisms, including bacteria, yeast, plants, and mammals. Most ADHs require zinc at the enzyme active site. ADHs are divided into three classes based on their monomer chain length (*2*). Of interest in the present paper are the class I enzymes, examples of which are horse liver and Baker's yeast ADHs. In terms of quaternary structure, the eukaryotic ADHs tend to be homodimers, whereas the prokaryotic ADHs usually are homotetramers. While there is a wealth of structural data on eukaryotic ADHs, it is only in recent years that crystal structures of bacterial and archaeal ADHs have been reported (*3*−*8*).

NAD^+-dependent alcohol dehydrogenase from *Bacillus stearothermophilus* strain LLD-R (htADH) is a homo-

[†] This work was supported by NIH Grant 5P20RR015588 to B.J.B. and NSF Grant NCB-13544b to J.P.K.

[‡] The atomic coordinates and structure factors (1rjw) for the structure of NAD^+-dependent alcohol dehydrogenase from *B. stearothermophilus* strain LLD-R have been deposited in the Protein Data Bank, Research Collaboratory for Structural Bioinformatics, Rutgers University, New Brunswick, NJ (http://www.rcsb.org).

* To whom correspondence should be addressed. Telephone: 302-831-0786. Fax: 302-831-6335. E-mail: bahnson@udel.edu.

[§] University of Delaware.

[||] University of California.

[⊥] University of Rochester.

[#] Present address: Center for Structural Biology, Yale University, New Haven, CT 06520.

[£] Present address: Laboratory of Structural Microbiology, Rockefeller University, New York, NY 10021.

[1] Abbreviations: ADH, alcohol dehydrogenase; htADH, NAD^+-dependent alcohol dehydrogenase from *Bacillus stearothermophilus* strain LLD-R; EcADH, NAD^+-dependent alcohol dehydrogenase from *Escherichia coli*; CbADH, $NADP^+$-dependent alcohol dehydrogenase from *Clostridium beijerinkii*; TbADH, $NADP^+$-dependent alcohol dehydrogenase from *Thermoanaerobacter brockii*; SsADH, NAD^+-alcohol dehydrogenase from *Sulfolobus solfataricus*; BaKR, $NADP^+$-dependent ketose reductase from *Bemisia argentifolii*; HLADH, horse liver alcohol dehydrogenase; ADH-T, alcohol dehydrogenase from *Bacillus stearothermophilus* strain NCA 1503; NAD^+, nicotinamide adenine dinucleotide; $NADP^+$, nicotinamide adenine dinucleotide phosphate; NCS, noncrystallographic symmetry; RMSD, root-mean-square deviation; PDB, Protein Data Bank; TFE, trifluoroethanol; CHESS, Cornell High-Energy Synchrotron Source; ADSC, Area Detector Systems Corporation; CCD, charge-coupled device; C_α, α carbon; DTT, dithiothreitol; PEG, poly(ethylene glycol); HEPES, 4-(2-hydroxyethyl)piperazine-1-ethanesulfonic acid; DEAE, diethylaminoethyl; KPi, potassium phosphate buffer.

10.1021/bi049736p CCC: $27.50
Published on Web 04/16/2004

tetrameric enzyme with a molecular mass of 36 338 Da and 339 amino acid residues per subunit. It shares about 31% of its sequence identity with horse liver alcohol dehydrogenase (HLADH). Just as in HLADH and other mammalian dimeric ADHs, htADH has two zinc atoms per subunit. One of these is responsible for the catalytic function of the enzyme, while the other adopts a structural role. The enzyme source organism, *B. stearothermophilus* strain LLD-R, has an optimum growth temperature of 75 °C and is classified as a moderate thermophile. Thermophilic enzymes have been studied extensively for the purpose of assessing their potential use as high-temperature biocatalysts in organic syntheses (*9*, *10*). A search has ensued to better understand the structural features, which confer enhanced thermostability, on these proteins in the hope of using protein engineering to produce biocatalysts with improved properties (*11*, *12*).

Now generally observed in many enzyme-catalyzed hydrogen-transfer reactions, the incorporation of quantum mechanical tunneling parameters are necessary to explain experimental kinetic data that accurately compare the rate constants of hydrogen-, deuterium-, and tritium-labeled substrates and their temperature dependence (*13*). The ADH enzyme system has developed as a paradigm for the study of the protein-mediated factors that control hydrogen tunneling (*14*). Site-directed mutagenesis of HLADH has allowed the expression of quantum behavior (*15*) and even suggested a structural and possibly a dynamic role for the tunneling component of the hydride transfer (*16*, *17*). This developing wealth of experimental data in the ADH system has prompted several groups to formulate theoretical methods to correlate ADH kinetics, structures, and dynamics (*18*−*22*). When the ADH is moved to a thermophilic form, the observation of tunneling in the htADH enzyme was shown to correlate with a functionally relevant protein dynamic transition that happens at ∼30 °C (*23*, *24*). These previous studies provide experimental evidence for a role of thermally excited enzyme fluctuations in modulating enzyme-catalyzed bond cleavage. What is lacking is an atomic-resolution structure to relate to the dynamics involved.

Here, we report the three-dimensional structure of a substrate−alcohol binary complex of alcohol dehydrogenase from *B. stearothermophilus* strain LLD-R at a resolution of 2.35 Å. This complex offers the first step toward a structural picture of functionally relevant dynamic behavior. We compare and contrast the structure to available homologous tetrameric ADHs and to a representative mammalian dimeric ADH, HLADH. The most intriguing insight into the enhanced thermostability and associated temperature-dependent kinetic behavior of htADH is obtained by comparing htADH to its nearest available structural homolog, mesophilic EcADH. We also report the amide hydrogen−deuterium (H/D) exchange data of htADH with and without NAD^+ bound, as studied by mass spectrometry. The H/D exchange results reveal that alterations in the exchange rates, which are linked to conformational changes upon NAD^+ binding, occur not only in the inferred cofactor pocket, but also in some regions that do not appear to be directly involved in cofactor binding.

EXPERIMENTAL PROCEDURES

Cloning, Expression, and Purification of htADH. Cloning, expression, and purification of htADH were originally carried out following the procedures of Cannio et al. (*25*) and Guagliardi et al. (*26*). Subsequently, the htADH gene was amplified directly by PCR from the genomic DNA of *Bacillus stearothermophilus* strain LLD-R (NCIMB 12403) and ligated into the expression vector pET-24b(+) to give the plasmid pET-ADH, as described elsewhere (*27*).

The expression and purification was carried out following the reported procedure (*25*) with minor modification. The enzyme htADH was overexpressed in *Escherichia coli* BL21 (DE3) cells. The cells were grown for 24 h at 37 °C, harvested, lysed, and centrifuged. The supernatant was heated at 65 °C for 15 min and again centrifuged to remove insoluble material. The supernatant was first passed through a fast flow DEAE-Sepharose column (Amersham Biosciences), and the fractions with ADH activity were pooled, concentrated, and passed through a Sephacryl S300-HR column (Amersham Biosciences). The enzyme was further purified by affinity chromatography using an Affi-Gel blue column (Biorad) and eluted with a salt gradient. The final yield was ∼9 mg/L of culture with a specific activity of 380 units/mg (60 °C). The homogeneity of the purified recombinant enzyme was confirmed by SDS−PAGE.

Protein Crystallization and Data Collection. The enzyme htADH was placed in a small 10-mL pressure cell with a YM30, 30 kDa cut-off membrane (Amicon). The protein was exchanged into a 20 mM potassium phosphate buffer (KPi) and 4 mM DTT (pH 7) at 4 °C for approximately 4 h under argon gas, with repeated additions of the exchange buffer. The exchanged sample was then concentrated under the same conditions to a concentration of 20 mg/mL. Protein crystallization conditions were obtained by hanging drop vapor diffusion using commercially available screens (Hampton Research). Drops were prepared at 25 °C by mixing 2 μL of the protein stock solution with an equal volume of the well solution. One condition was found to grow crystals, which was optimized to a final crystallization condition of 12% trifluoroethanol, 12% PEG 4000, and 100 mM HEPES (pH 7.5) at 25 °C.

Diffraction data were collected using an ADSC Quantum-4 CCD detector on beam line A1 at the CHESS synchrotron. The detector distance was set at 200 mm, and an X-ray wavelength of 0.908 Å was used. The data collection temperature was −180 °C. Crystals were transferred to a cryo buffer containing 25% (v/v) PEG 400, flash-cooled in a pool of liquid nitrogen, and then mounted on the goniometer. The data were collected using 1° oscillation scans for a time interval of 20 s per frame. A total of 140 frames were collected from one crystal. Integrated reflection intensities were obtained from DENZO and scaled with SCALEPACK (*28*).

Crystal Structure Solution and Refinement. The diffraction data were indexed based on a primitive orthorhombic unit cell with cell dimensions $a = 68.3$ Å, $b = 138.2$ Å, and $c = 158.7$ Å. After the diffraction data were indexed, it appeared likely that there were four ADH subunits in the crystal asymmetric unit, implying a solvent content of about 50%. The crystal structure of htADH was solved by molecular replacement using a search model based on the crystal structure of NAD^+-dependent alcohol dehydrogenase from *E. coli*, EcADH (*3*). Coordinates for the crystal structure of the holo form of EcADH were obtained from Hans Eklund prior to Protein Data Bank (PDB) submission. This structure

consists of four subunits, three of which have a bound NAD^+ cofactor, while the remaining subunit is in an open (NAD^+-free) conformation (*3*). The tetramer has approximately 222 noncrystallographic symmetry (NCS). The search model was constructed by replacing the three closed subunits with open subunits. The newly modeled tetramer using the open subunits was generated from the original open subunit by applying the appropriate NCS operators. The final molecular replacement search model included this modeled tetramer of open subunits with all residues except glycine mutated to alanine.

A molecular replacement solution was obtained using AMoRe (*29*, *30*). The rotation map gave four peaks of height 6 σ that were higher by 2.5 σ than the next-highest peaks in the map. These four peaks were interpreted to represent the four orientations at which the search model would overlay an object with 222 NCS. Translation searches in the space group $P2_12_12_1$ for any of these orientations produced convincing solutions. The maximum peak height was 10−12 σ, and the next-highest peaks were lower by 3−4 σ than those of the best solutions.

Rigid-body refinement was run in CNS (*31*), starting from the final molecular replacement solution. Each subunit of the tetramer was refined as an independent rigid body. $R_{working}$ was 0.477 using a resolution range from 10 to 3 Å. Only minimal orientation changes of each subunit relative to the others were observed.

Density modification techniques (*32*−*35*) were applied to the crude molecular replacement phases using DM (*30*, *36*). Solvent flattening, histogram matching, and NCS averaging were performed. Phases were generated for all reflections (41.4−2.35 Å). A bulk solvent correction was applied using a solvent mask generated by CNS. The NCS operators were obtained by pair-wise overlays of one subunit (labeled subunit A) with each of the other three subunits (labeled B−D) in CNS. A monomer mask for averaging was generated in NCSMASK (*30*) by forming an atom mask around subunit A with an atomic radius of 3.0 Å. The solvent mask was generated by first surrounding the tetramer with a mask with an atomic radius of 3.0 Å. Then, this mask was extended, using the space-group symmetry operators, to fill a complete unit cell. Next, one cycle of DM was run, and the solvent mask internally generated by DM was output. Finally, these two masks were merged and examined in the program O (*37*). The mask was edited slightly so as to uncover a few internal regions, which were incorrectly assigned to the solvent region. A total of 25 cycles of density modification were run.

After the density modification procedures, the electron density maps were of reasonable quality and were used to build 290 of the 339 residues of subunit A. The starting model for building was the NAD^+-free subunit of EcADH superimposed onto subunit A of the rigidly refined tetramer. Each residue of the partially built model was mutated to that predicted by a hypothetical alignment of the *E. coli* sequence with that of the htADH title structure. The hypothetical alignment was obtained as follows. STAMP (*38*) was used to align the structure of EcADH with two closely related proteins: PDB (*39*) 1jvb, alcohol dehydrogenase from the archaeon *Sulfolobus solfataricus* (SsADH) (*7*); and 1e3j, ketose reductase (sorbitol dehydrogenase) from *Bemisia argentifolii* (BaKR), which was used to solve the *E. coli* structure (*40*). This composite alignment was then matched to the *B. stearothermophilus* strain LLD-R sequence using CLUSTALW (*41*). Finally, the alignment was cleaned up by taking out 1jvb and 1e3j and then pruning any gaps present in both the *E. coli* and *B. stearothermophilus* sequences. After subunit A was built, a complete tetramer was assembled by generating subunits B−D from subunit A using the NCS operators.

The tetramer was refined in CNS by simulated annealing using torsion-angle dynamics. Care was taken to ensure that the same test-set reflections were used in this step that were used in the rigid-body refinement step. NCS restraints were applied to the tetramer. All atoms were restrained using a restraint weight of 300 kcal/mol $Å^2$. After this, 30 cycles of individual temperature-factor refinement were run. NCS temperature-factor restraints were applied to all atoms of the tetramer. For these steps, $R_{working}$ and R_{free} (*42*) started out at 0.409 and 0.396, respectively, and dropped to 0.295 and 0.311, respectively, after refinement. A combined-phase electron density map was generated and used in the next round of model building. The density-modified phases were combined with those of the refined partial model. The combined-phase map was averaged using RAVE to strongly enforce the 222 noncrystallographic symmetry (*43*, *44*). This map showed reasonably clear connections filling all six sequence gaps in the structure. After building these regions, the model lacked only the two residues closest to the C terminal of each subunit. The model was refined again by simulated annealing, followed by temperature-factor refinement using CNS. The values of $R_{working}$ and R_{free} dropped to 0.261 and 0.276, respectively. An unaveraged combined-phase map and a purely model-phased map were used in the next round of model-building. These maps suggested that the NCS restraints were too tight in some regions. Pro^{56} was identified as a *cis*-proline and modeled accordingly. The two residues closest to the C terminal of each subunit were built into the difference density.

Trifluoroethanol (TFE) ligands, one per subunit, were identified in close proximity to the catalytic zinc atoms and added to the structure. Trial coordinates for TFE were obtained from PDB 1a71 (*45*). CNS and O database files were obtained from XPLO2D (*46*). In addition, nine TFE molecules were identified in the ordered solvent shell surrounding the tetramer.

Water molecules were placed during successive cycles of model building and refinement. Tentative locations were found from electron density difference maps (coefficients $F_o - F_c$). These locations were checked against the protein model using a $2F_o - F_c$ difference electron density map and an annealed $2F_o - F_c$ composite omit map. Putative water sites not residing in a significant omit map density or those too close to or too far away from protein atoms were rejected.

The noncrystallographic symmetry restrained model was fine-tuned during the final stages of refinement. Side chains were released from restraints if the electron density maps suggested that the restraint model did not apply to them. The structural and catalytic zinc atoms and their coordination spheres were not restrained. Residues 74−76 and the four residues closest to the C terminal were refined freely. In all, 2238 of the 2554 non-hydrogen atoms of each subunit were restrained. To determine the appropriate restraint weight, a

series of simulated annealing runs was made as the restraint weight was varied from 0 to 300 kcal/mol Å^2. The best R_{free} occurred when the restraint weight was 50 kcal/mol Å^2. This was the restraint-weight value used to bring the refinement to convergence.

The final model of htADH had 4 subunits of 339 amino acid residues each, both a structural and a catalytic zinc atom per subunit, 1 TFE ligand per subunit active site, 9 TFE molecules remote from the active site, and 332 ordered water molecules. A final $2F_o - F_c$ annealed composite omit map for this model was used to confirm the validity of the chain trace and the final model. The final $R_{working}$ and R_{free} values were 0.214 and 0.252, respectively.

Structure Rendering and Analysis. Structurally corrected sequence alignments were performed with STAMP (*38*) and displayed using ALSCRIPT (*47*). Secondary-structure assignments were made using DSSP (*48*). Structure superpositions were calculated using LSQKAB (*30*, *49*). Salt-bridge interactions were obtained from CONTACT (*30*). Figures 1, 3, and 5 were made using MOLSCRIPT (*50*), POVSCRIPT (E. Peisach and D. Peisach), and POVRAY (www.povray.org). The electron density contours in Figure 3 were produced using CNS (*31*), CCP4 (*30*), and RAVE (*43*, *44*). Structure stereochemistry and data quality were validated using PROCHECK (*30*, *51*) and SFCHECK (*30*, *52*), respectively.

Amide H/D Exchange by Mass Spectrometry. Peptides used for H/D exchange analysis were identified by MS/MS sequencing conducted "on-the-fly" as peptides eluted from the capillary column, as described previously (*53*). The exchange reactions were initiated by adding 10 μL of a newly thawed protein solution (~0.5 mg/mL, 50 mM KPi at pH 7.4, 250 mM KCl, and 2.5 mM DTT) with or without 100 mM NAD^+ to 90 μL of D_2O. After the incubation at 10 °C, the exchange reaction was quenched by lowering the pH to 2.4 and the temperature to 0 °C and was followed by pepsin digestion of the protein. The resulting peptides were analyzed on a reversed-phase capillary column (POROS 20 R1, PerSeptive) coupled to a QStar Pulsar quadrupole time-of-flight mass spectrometer with a normal electrospray interface (PE Biosystems). The maximum time from the initiation of digestion to the elution of any peptide was 22 min. Zero time point controls (the "artifactual in-exchange" control) were performed by adding a quench buffer to the protein solution prior to the exposure to D_2O. Measured peptide masses were corrected for artifactual in-exchange at $t = 0$, normalized to 100% D_2O, and corrected for back-exchange following the method described by Resing et al. (*53*). Typically, 12 data points were collected with the shortest incubation time of 7 s and the longest incubation time of 130 min. Kinetics of exchange using corrected peptide masses were fit by NLSQ to the equation: $Y = N - Ae^{-k_1 t} - Be^{-k_2 t} - Ce^{-k_3 t}$, where N is the total number of amides exchanging over the observed time course for each individual peptide, and A, B, and C correspond to the number of amides exchanging with rate constants k_1, k_2, and k_3, respectively. The enzyme is in its native state under the H/D exchange conditions. The rate constants k_1, k_2, and k_3 have been measured under EX2 conditions, so that what is measured is the equilibrium between the open and closed forms of the protein [$k_{obs} = (k_{open}/k_{close}) \times k_{ex}$]. The number of nonexchanging amide hydrogens is calculated by subtracting the number of exchanging amides ($A + B + C$) from the total number of backbone amides (N_H) in the peptide, excluding the proline residues.

Table 1: htADH Crystallographic Refinement and Model Statistics

Data Collection	
resolution range (Å)	41.4−2.35
completeness (%)	87.5
unique reflections	51 591
R_{merge}[a]	0.068
Refinement	
subunits/asymmetric unit	4
protein atoms	10 216
heteroatoms	86
solvent atoms	332
average temperature factor (Å^2)	37.9
$R_{working}$[b]	0.214
R_{free}[b]	0.252
RMSD from Ideal Geometry	
bonds (Å)	0.007
angles (deg)	1.30
dihedrals (deg)	23.60
impropers (deg)	0.85
Ramachandran Plot	
core (%)	91.3
allowed (%)	8.2
generously allowed (%)	0.4
disallowed	none
Estimated Coordinate Error[c]	
from Luzzati plot (Å)	0.36
from σ_A (Å)	0.28

[a] $R_{merge} = \Sigma|I_o - I_a|/\Sigma|I_a|$, where I_o is the observed intensity and I_a is the average intensity, with the sums being taken over all symmetry-related reflections. [b] R factor $= \Sigma|F_o - F_c|/\Sigma|F_o|$, where F_o is the observed amplitude and F_c is the calculated amplitude. R_{free} is the equivalent of $R_{working}$, except it is calculated for a randomly chosen set of reflections (5%) that were omitted from the refinement process (*42*). [c] Error estimates are based on R_{free}. The methods of Luzzati (*68*) and Read (*69*), respectively, were used.

RESULTS

The tetrameric structure of htADH is the first structure solved of ADH from *B. stearothermophilus*. The structure shares many similarities with other ADH structures. The closest match is the *E. coli* ADH, with which it shares 55% identity. The structure reported is a binary complex with the alcohol−substrate analogue TFE. Refinement and model statistics are shown in Table 1. The high quality of the model is supported by a reasonable R factor, clear and fully interpreted electron density maps, and a stereochemical quality supported by favorable Ramachandran plot results (Table 1). The structural features that highlight its similarities and differences with other ADHs will be summarized below. Furthermore, the title structure allows site-specific interpretation of amide H/D exchange data to be interpreted. Here, the impact of cofactor binding is presented, making predictions regarding the, as yet, unsolved structure of the binary complex of htADH with NAD^+.

Quaternary Structure of htADH. A ribbon diagram of htADH is shown in Figure 1. The enzyme is a homotetramer where the subunits are related by three mutually perpendicular 2-fold molecular axes. The axes are parallel to the horizontal, vertical, and normal directions of the drawing. The axis normal to the drawing relates the subunit pairs A/D and B/C. The quaternary structure is thus a dimer of these

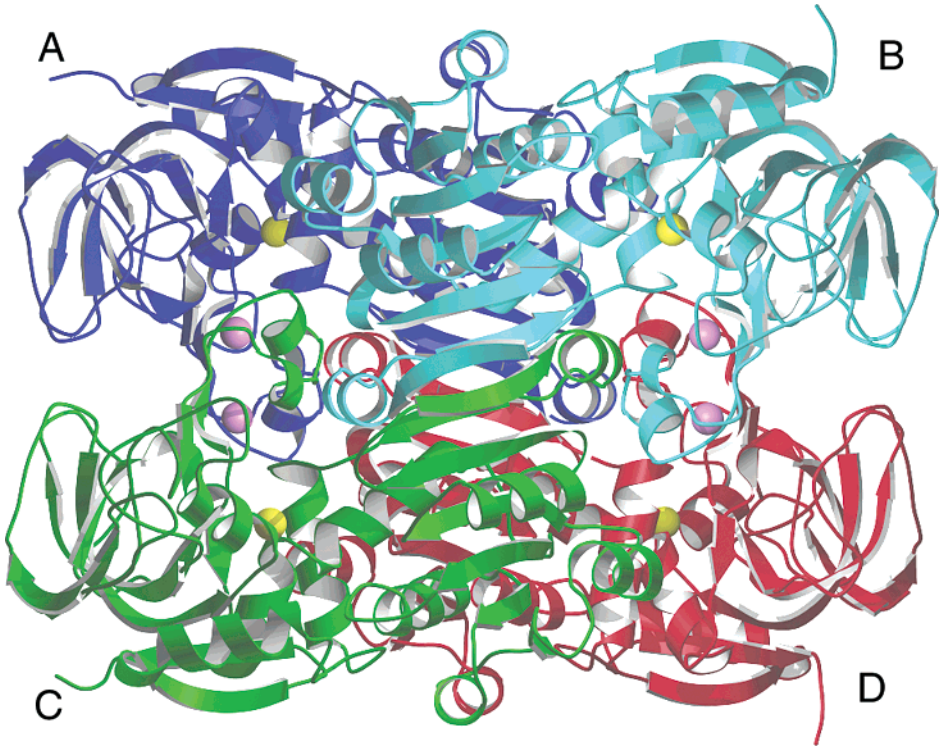

FIGURE 1: Ribbon diagram for htADH. Subunits A−D are colored blue, turquoise, green, and red, respectively. Dimers similar to HLADH are formed by the subunit pairs A/D and B/C. Catalytic zinc atoms are colored yellow, and structural zinc atoms are colored magenta. The 222 NCS axes lie along the horizontal, vertical, and normal directions of the figure view.

subunit pairs. Furthermore, the tertiary structure of the A/D or B/C dimers is highly similar to the dimeric mammalian ADH enzymes (*54*). Contacts between the subunit pairs A/C and B/D are mediated by the loops surrounding the structural zinc atoms, which are colored in magenta. Hence, the structural zinc atom binding loops play a role in enzyme oligomerization.

As is the case with each of the homologous ADHs, the subunit of the title structure is divided into two functionally different domains. Residues 150−285 comprise the cofactor-binding domain, while residues 1−149 and 286−339 fold into the catalytic domain. The two domains are separated by a deep cleft that spans the entire width of the subunit. Near the bottom of this cleft is the catalytic zinc atom, shown in Figure 1, colored in yellow. Each cofactor domain pairs tightly with that of a neighboring subunit, resulting in extended β sheets, which run along the front and back sides of the tetramer and whose β strands stack roughly parallel to the vertical axis of Figure 1. The subunit pairs forming these extended β sheets are the dimers mentioned above that are similar to dimeric mammalian ADHs.

Comparison to Other Tetrameric Alcohol Dehydrogenases. The structures of a number of tetrameric ADHs have been published, to which the title structure may be compared. There are an apo, a holo, and a mutant form of ADH from *Clostridium beijerinkii* (CbADH), PDB 1ped, 1kev, and 1jqb, respectively (*4*, *5*, *8*); $NADP^+$-free and $NADP^+$-bound forms of ADH from *Thermoanaerobacter brockii* (TbADH), PDB 1bxz and 1ykf, respectively (*4*−*6*); NAD^+-free and NAD^+-bound forms (in the same crystal) of holo-EcADH (*3*); the apo form of SsADH (*7*); and the apo form of BaKR (*40*). Also included for comparison purposes are apo and holo forms of a representative dimeric mammalian ADH, HLADH, PDB 8adh and 2ohx, respectively (*54*, *55*). A composite structurally corrected sequence alignment (Figure 2) of these structures identified 190 residues that were structurally equivalent and hence constitute a conserved core of the ADH fold. The lone mammalian sequence in Figure 2 stands out with two significant insertions compared to the bacterial enzymes. Compared with the title structure, the RMSD for the C_α atoms of the protein core afford the following similarity ranking: NAD^+-free EcADH, 0.86 Å; NAD^+-bound EcADH, 1.16 Å; apo-SsADH, 1.34 Å; apo-HLADH, 1.39 Å; apo-BaKR, 1.48 Å; $NADP^+$-free TbADH, 1.80 Å; apo-CbADH, 1.80 Å; $NADP^+$-bound TbADH, 1.82 Å; holo-HLADH, 1.88 Å; and holo-CbADH, 1.95 Å.

The tetrameric enzymes can be divided into two groups based on their zinc content. HtADH, EcADH, SsADH, and BaKR have both structural and catalytic zinc atoms, while TbADH and CbADH have the catalytic zinc atom but lack the structural zinc atom. In all but one of the structures of the former group, the structural zinc atom showed tetrahedral coordination by four cysteine residues. The exception is SsADH, where a glutamate residue replaces one cysteine (Figure 2). The most common coordination of the catalytic zinc atom is the type first observed in HLADH, where three of the four ligands are Cys^{38}, His^{61}, and Cys^{148} (htADH numbering). In CbADH and TbADH, the final cysteine residue is replaced by aspartate. In BaKR, the glutamate residue adjacent to His^{61} replaces the final cysteine residue as the third ligand. In EcADH, SsADH, CbADH, and TbADH, this same glutamate can serve as the fourth zinc ligand, displacing a water molecule normally present in cofactor-free enzyme subunits (*3*).

A notable difference among the compared structures is the variation of the conformation at Pro^{56} (htADH numbering) and equivalent residues. This proline was refined as a *cis*-proline. Although this residue lies within a structurally

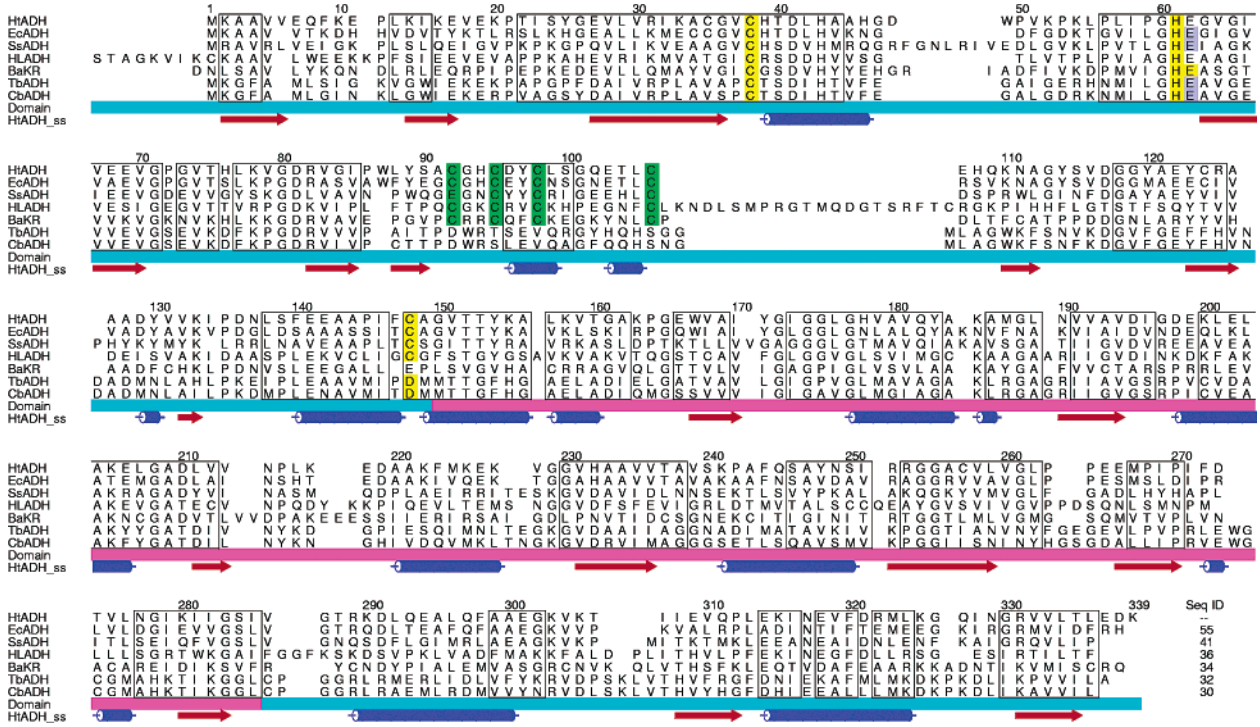

FIGURE 2: Structurally corrected sequence alignment of ADH. The htADH sequence is on top, and its secondary structure is aligned on the bottom. Numbering is based on the htADH sequence. The catalytic domain is colored turquoise and the cofactor domain is colored magenta. Residues binding the catalytic and structural zinc atoms are colored yellow and green, respectively. Glutamate residues, which have been observed to bind the catalytic zinc atom as a fourth ligand, are colored purple. Boxes enclose the 190 structurally equivalent residues used for aligning sequences by STAMP (*38*). The column labeled "Seq ID" at the end of the alignment reports the sequence identity of the ADH sequences relative to the htADH sequence. The alignment was prepared using STAMP (*38*) and displayed using ALSCRIPT (*47*).

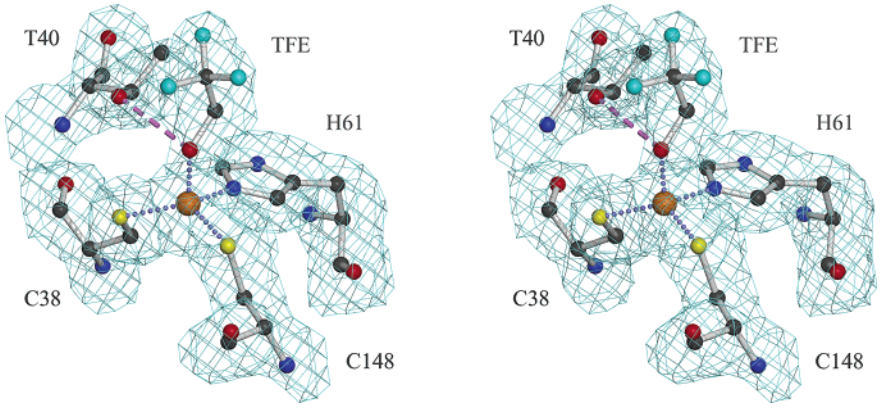

FIGURE 3: Catalytic Zn site of htADH. The catalytic Zn atom, colored orange, is in a distorted tetrahedral coordination by side-chain heteroatoms of residues Cys[38], His[61], and Cys[148]. The alcoholic oxygen of the substrate analogue TFE occupies the fourth site in the coordination sphere. Coordination distances range from approximately 2.0 to 2.5 Å. The hydroxyl oxygen of Thr[40] (dashed line) is presumed to mediate the proton abstraction from the substrate during catalysis. The electron density is from the final NCS-averaged $2F_o - F_c$ annealed composite omit map contoured at 1.5 σ.

similar region of the alignment of homologous ADH structures (Figure 2), there is a great deal of variation at this position. Three of the homologous structures also have proline in this position, but for only two of these, HLADH and SsADH, the proline adopts a cis conformation.

Alcohol−Substrate Binding in the Active Site. The title structure is a binary complex lacking the NAD^+ cofactor. Protein crystal screening is currently underway to obtain a closed form ternary complex structure. It is important to note that the binding of the substrate analogue TFE in the active site has not caused the enzyme subunit conformation to close. This is apparent from the structure similarity ranking of various ADH structures relative to htADH (see above). In pair-wise comparisons, the similarity of the conformation of htADH is consistently closer to the cofactor-free form of each protein than to the corresponding cofactor-bound form. Figure 3 is a plot of the enzyme active site showing the catalytic zinc atom, its coordination sphere, and Thr[40], which is expected to play an important role in catalysis. The zinc coordination environment is a distorted tetrahedron. Three of the zinc ligands are those expected from the alignments with mammalian ADHs, namely, side-chain heteroatoms of Cys[38], His[61], and Cys[148]. The oxygen of the substrate analogue TFE occupies the fourth coordination position. The hydroxyl group of Thr[40] lies within 3.3 Å of this oxygen. In the proposed enzyme mechanism (*56*), the proton on the alcoholic oxygen is transferred first to the Thr[40] hydroxyl group, then to the 2′-hydroxyl group of the nicotinamide

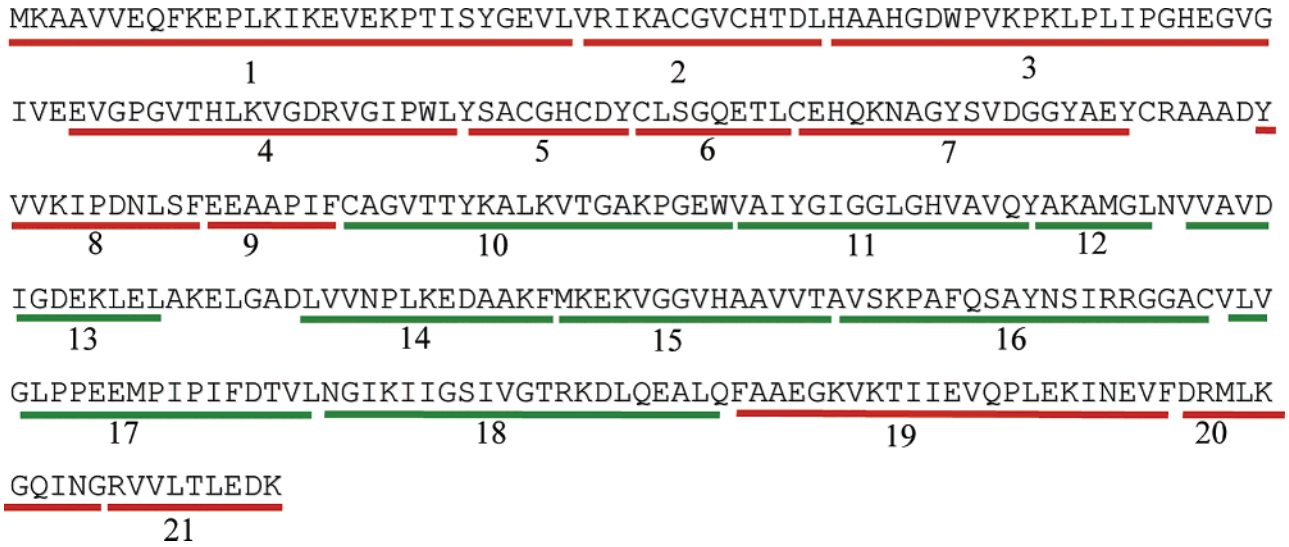

FIGURE 4: Primary sequence of htADH with the peptide fragments labeled. A total of 21 peptides generated by pepsin digestion are numbered starting from the N terminus. Peptides located in the cofactor-binding domain are colored green, and peptides located in the substrate-binding domain are colored red.

ribose of the cofactor, then to Nϵ2 of His[43], and finally to the solvent.

Alternate Catalytic Zinc Site Observed in Two Subunits. At the completion of the htADH structure analysis, a final $F_o - F_c$ difference map was calculated to search for extreme values of residual positive or negative electron density. Normally, these peaks and holes indicate regions that may need to have the model built in or deleted, respectively. Two features worth noting are 2−2.5 Å from the catalytic zinc atom of either subunit A or C. The peaks stand out as the most pronounced features of the map. Overlays of the open subunit of holo-EcADH onto either subunit A or C suggest that each of these peaks represents an alternative zinc site of low partial occupancy, where the fourth zinc ligand is Glu[62]. Partial zinc occupancy was also suggested by comparing the catalytic zinc temperature factors for all four subunits. Those for subunits A and C are above 50 Å^2, while that for B is below 30 Å^2 and that for D is below 40 Å^2. Because of the resolution limitations of the X-ray diffraction data to 2.35 Å, the alternate conformations suggested were not refined and therefore were not presented in the final model submitted to the PDB.

Amide H/D Exchange by Mass Spectrometry. H/D exchange was performed at 10 °C with and without NAD^+ (10 mM) present, and the exchange experiments and data analysis were carried out following the procedures described above. The independent activity assay confirmed that the enzyme is fully active after incubation for 150 min under the exchange conditions. A total of 21 nonoverlapping peptides generated by pepsin digestion have been identified for H/D exchange analysis (Figure 4). The H/D exchange described here only measures deuteration at backbone amides, because side-chain deuterons will back-exchange to hydrogen during LC/MS. For each peptide, the number of incorporated deuterons was obtained by calculating the difference between the weighted average mass of the peptide before and after H/D exchange. The plots of incorporated deuterons versus time were fitted with a three-exponential model to give the exchange rate constants k_1, k_2 and k_3 and the number of corresponding exchanging hydrogens. On the

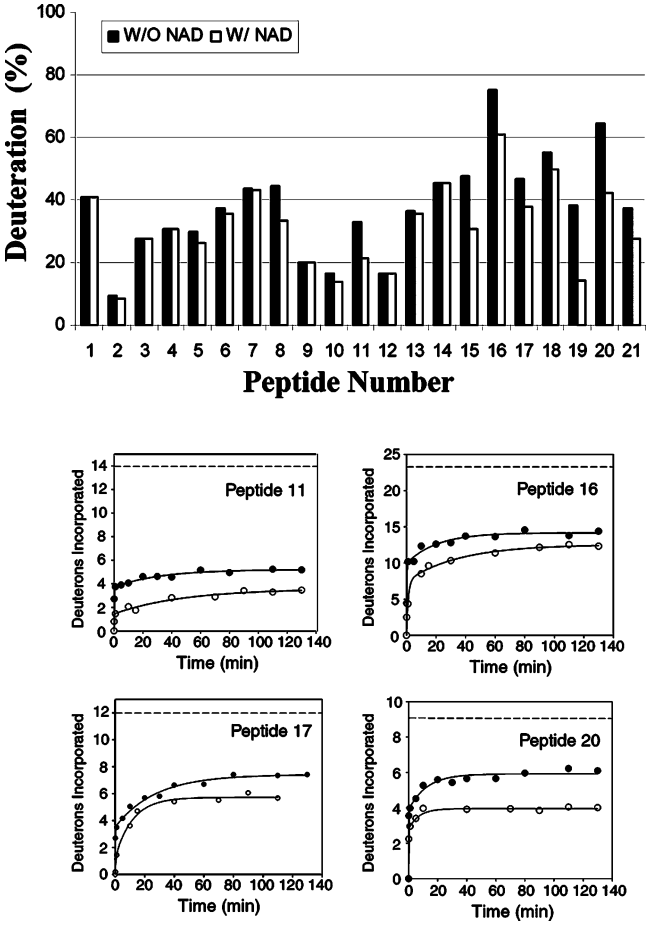

FIGURE 5: (Top) Percentage of deuteron incorporation for each peptide at the end of the H/D exchange measurement (130 min). (Bottom) H/D exchange time-course plots for four representative peptides that displayed a decreased deuteron incorporation upon NAD^+ binding [ligand-free htADH (●), htADH and 10 mM NAD^+ (○)]. The dashed lines indicate the number of maximum exchangeable amide hydrogens within each peptide.

basis of their exchanging rates, the amide hydrogens can be categorized into three groups: fast-exchanging hydrogens

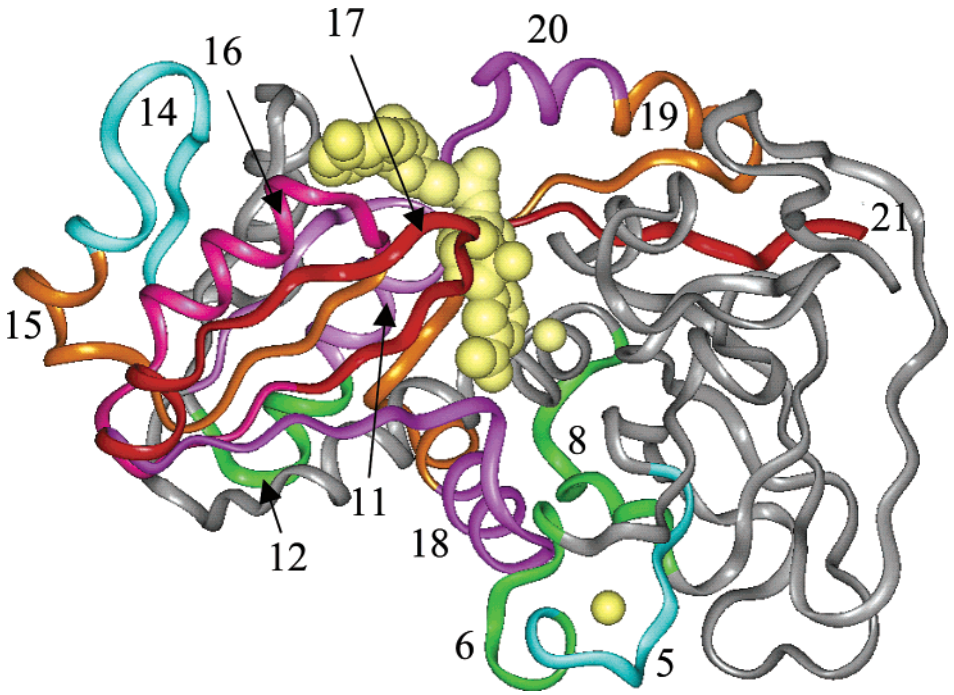

FIGURE 6: H/D exchange displayed on htADH monomer. The two zinc ions and the modeled-in cofactor NAD^+ are colored yellow. The cofactor-binding domain is on the left, and the substrate-binding domain is on the right. Peptides exhibiting a decrease in the deuteron incorporation level or H/D exchange rate upon NAD^+ binding are labeled and colored. Peptides, which bind the cofactor, are colored orange (15, 19), pink (16), red (17, 21), and magenta (11, 18, 20). Peptides that are not directly involved in cofactor binding are colored green (6, 8, 12) and blue (5, 14). Peptides exhibiting no change in deuteron incorporation level are colored gray.

(k_{ex} > 1 min^{-1}), intermediate-exchanging hydrogens (0.1 min^{-1} < k_{ex} < 1 min^{-1}), and slow-exchanging hydrogens (k_{ex} < 0.1 min^{-1}).

A total of 13 of the 21 peptides display changes upon htADH binding of NAD^+, including nine peptides that show a decreased deuteration level and four peptides that show a decreased exchange rate (top of Figure 5). The exchange time-course plots for four of the nine peptides showing decreased deuteration level are shown in Figure 5 (bottom). Most of the nine peptides are from the putative regions that are involved in cofactor binding, including four peptides located in the cofactor-binding domain (peptides 11, 15−17) and three located in the substrate-binding domain (peptides 19−21), as shown in Figure 6. However, there are two peptides (peptides 5 and 8) that are not in direct contact with the cofactor and that also show a decrease in the deuteration level. The time-course plots for the four peptides that exhibit decreased exchange rates are shown in Figure 7. On the basis of the crystal structure, peptide 18 is located at the bottom of the cofactor-binding pocket, whereas peptides 6, 12, and 14 appear not to be in any direct contact with the cofactor (Figure 6). The remaining eight peptides, which are mainly located in the substrate-binding domain, display almost identical deuteration levels and rates before and after NAD^+ binding (see data in the Supporting Information).

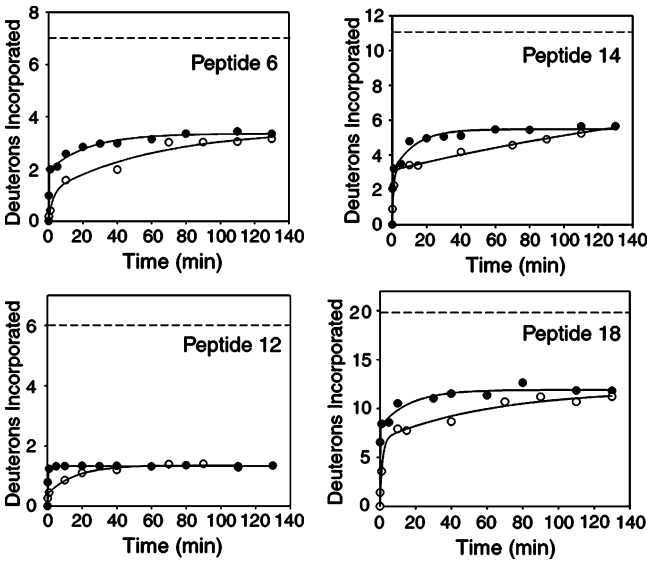

FIGURE 7: Amide H/D exchange time-course plots for the peptides that displayed slower exchange rates upon NAD^+ binding. The dashed lines indicate the number of maximum exchangeable amide hydrogens within each peptide [free htADH (●), htADH and 10 mM NAD^+ (○)].

DISCUSSION

The comparison of the protein structure and function for a specific enzyme from thermophilic, mesophilic, and even psychrophilic sources has gained a great deal of interest from practical protein engineering (*57*) to basic science questions (*58*). This comparison in the ADH system now allows a structural perspective to be developed that helps explain previous observations that link thermally driven protein fluctuations and functions (*23*, *24*, *27*). The structure of a binary complex structure of htADH from the thermophilic organism *B. stearothermophilus* and its comparison to the homologous mesophilic ADH from *E. coli* is the first step toward understanding this dynamic−function link.

"Open" Versus "Closed" Subunit Conformation. It has been observed that cofactor binding in an ADH subunit induces a change in the conformation of the catalytic domain relative to the cofactor domain. The catalytic domain rotates so as to partially close the cleft separating it from the

Table 2: Open/Closed Conformational Change for ADH Enzymes[a]

	cofactor domain fit RMSD (Å)	catalytic domain fit RMSD (Å)	ω (deg)	ϕ (deg)	χ (deg)	$t_{\|\|}$ (Å)	open form PDB	closed form PDB
			Open/Closed[b] Form Pairs					
HLADH	0.430	0.304	94.14	76.44	9.66	−0.201	8adh	2ohx
EcADH	0.520	0.482	84.03	83.45	12.21	−0.484	n. a.	n. a.
TbADH	0.272	0.378	113.08	127.78	1.86	0.163	1bxz	1ykf
CbADH	0.374	0.453	97.04	−1.08	0.99	−0.946	1ped	1kev
			Closed Form HLADH[c] as a Reference					
NAD$^+$-free htADH	1.417	1.001	96.54	61.60	15.54	−0.888	1rjw	2ohx
NAD$^+$-free EcADH	1.389	1.075	97.82	72.92	18.95	−0.891	n. a.	2ohx
Apo-SsADH	1.517	1.566	94.52	53.55	18.96	0.090	1jvb	2ohx
Apo-BaKR	1.248	1.369	109.65	61.24	19.75	−0.184	1e3j	2ohx
NADP$^+$-free TbADH	1.295	1.612	104.58	60.24	9.64	0.641	1bxz	2ohx
Apo-CbADH	1.273	1.557	96.14	49.40	8.36	0.310	1ped	2ohx

[a] The basis vectors of the reference Cartesian coordinate system for these calculations are parallel to the 222 NCS axes of htADH. The *x*, *y*, and *z* axes depicted in Scheme 1 are parallel to the molecular axes relating subunits A and C, A and B, and A and D, respectively. To start the calculation, the coordinates of the atoms of each cofactor-bound subunit were expressed in the reference Cartesian system. Then the domain superpositions were performed as described in the text. Cofactor and catalytic domain fits were based on 89 and 101 structurally equivalent C_α atoms, respectively. The angles ω and ϕ express the domain rotation axis in spherical coordinates and are depicted in Scheme 1. The value ω is the angle between the rotation axis and the *z* axis. The angle between the *x* axis and a projection of the rotation axis onto the *xy* plane is defined as ϕ. The extent of open/closed-domain rotation that relates the movement of the catalytic domain is given by χ, and the translation of the superposed domain parallel to the rotation axis is given by $t_{\|}$. [b] Open and closed forms of each ADH listed were compared. [c] The open form of each listed ADH structure was compared to the closed-form structure of HLADH.

Scheme 1: Definition of the Domain Rotation Axes for the Values Presented in Table 2

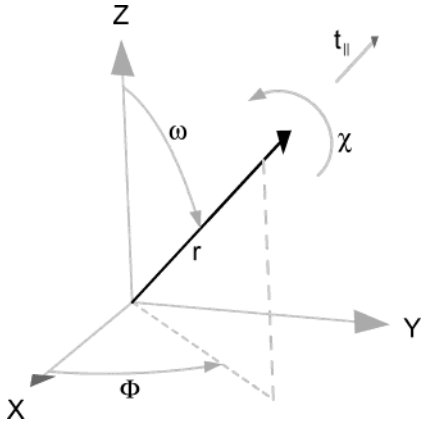

cofactor-binding domain. This conformational change has been explained by a necessity to ensure a hydrophobic environment in the active site, thereby facilitating hydride transfer from the substrate to the nicotinamide ring of the cofactor (*56*, *59*). To characterize this conformational change for htADH relative to the other ADHs, each domain is treated as an independent rigid body. For any pair of subunits to be compared, the cofactor domains are lined up; from this orientation, the catalytic domains are then superposed. The rigid-body motion for the last step represents the change in the conformation upon cofactor binding. The domain superposition results are presented in Table 2. In the upper part of the table, those structures where both open- and closed-form structures are available are shown. The title structure htADH is not included here because a closed-form structure has not yet been solved. Here, the closed-form structure of each listed ADH is the reference structure, and its corresponding open-form structure is fit to it. The magnitude of the catalytic domain rotation, given by the parameter χ, suggests that there is no clear pattern relating these four cases. Dimeric HLADH and tetrameric EcADH undergo extensive domain rotations of no less than about 10°, while TbADH and CbADH show very little rotational motion. In the lower part of the table, the holo form of HLADH is the reference structure for each superposition, and the open forms of the structures listed are fit to it. This comparison allows an estimate of the magnitude of the conformational change associated with an open/closed transition for htADH. These calculations are less precise than those given above, as evidenced by the higher RMSD values for the atoms used for fitting. Nevertheless, the ranking of the χ values should coincide roughly with the relative extent of domain rotation expected in each case. On the basis of this, we conclude that the domain rotations for SsADH and BaKR would be more like that of EcADH than those of CbADH or TbADH. It is our prediction that the domain rotation for the title structure htADH will be between these extremes but closer to that of EcADH.

Mechanistic Importance of the Binary TFE Complex. An overlay of holo-HLADH with the title structure suggests that TFE is bound unproductively, in the sense that the pro-R hydride would be pointing away from the C_4 atom of the nicotinamide ring. This has been observed before, in a ternary complex of HLADH, NAD$^+$, and bromobenzyl alcohol (*56*). In that study, the authors show by modeling that ligand rotation could bring the pro-R hydrogen within 3 Å of the nicotinamide ring, a requirement for efficient hydride transfer during catalysis. When the pro-R hydrogen is rotated to this position, no steric clashes with protein side chains are created. The situation with the title structure is analogous to that of the HLADH ternary complex. A model of the TFE rotation (data not shown) demonstrates that the ligand could be brought into a productive binding mode without generating any bad contacts with the enzyme.

A binary alcohol−substrate complex would be considered an unproductive complex for HLADH, which is known to have an ordered dehydrogenase mechanism, where cofactor binding precedes substrate−alcohol binding (*1*). However,

the htADH enzyme has been shown to follow a random equilibrium kinetic mechanism (Kohen and Klinman, unpublished), such that a binary alcohol complex is expected to lie somewhere along the mechanistic trajectory of the enzyme. The structural comparison of open and closed ADH structures, discussed above and presented in Table 2, definitively shows that the NAD^+-free TFE−htADH complex is predominantly an open-form structure. Here, it is predicted that upon binding of the NAD^+ cofactor, the htADH structure will be close to its catalytically active form.

It is likely that both NAD^+-free and NAD^+-bound forms of htADH are each an ensemble of open and closed conformations, with the distribution of these conformations in the crystallographically observed structure depending on their relative free energy. This can be inferred from the X-ray data analysis, in which alternate structural forms of htADH appear to exist in a close free energy balance. In two subunits of the tetramer, difference electron density peaks are consistent with a minor conformation of the active site in which the zinc-bound TFE is replaced by a coordination to Glu^{62}. Glutamate-coordinated zinc has been observed in other ADHs. Karlsson et al. (*3*) have argued that the replacement of glutamate for the zinc-bound water may be a necessary step prior to substrate−alcohol binding. It should be noted that all ADH sequences aligned in Figure 2 have a Glu residue at the position analogous to Glu^{62} of htADH, thereby highlighting its probable functional importance. The crystallographic evidence observed for htADH suggests that the classical zinc-binding environment and the newly observed glutamate-coordinated zinc may be nearly isoenergetic and of functional significance.

Amide H/D Exchange of Free and NAD^+-Bound Enzymes. Considering that the dissociation constant of htADH for NAD^+ at 10 °C is 0.72 ± 0.08 mM as measured by fluorescence-quenching titration (*27*), about 93% of the enzyme will form a complex with NAD^+ and will be in the closed form in the presence of 10 mM NAD^+. The fact that the peptides (peptides 11 and 15−18) displaying the greatest decreases in the deuteration level or exchange rate upon cofactor binding are from the regions responsible for NAD^+ binding confirms the dominating role of the nucleotide-binding domain in cofactor binding. Peptides 19−21, which are located in the alcohol−substrate-binding domain and form the "lid" of the NAD^+-binding pocket, also exhibit substantial decreases in their deuteration level. The decreases in the deuteration level or exchange rate for these peptides are due to the protection effect of domain closure and NAD^+ binding, which prevents the access of the solvent to the amide hydrogens. However, an unexpected observation is that some peptides (peptides 5, 6, 8, 12, and 14), which appear not to be in direct contact with the cofactor, also show decreases in their deuteration level or exchange rate. This cannot be explained by the protection effect of the cofactor as shown in Figure 6. The decreases must be caused by some concomitant changes in the local structure and dynamics accompanying the open/closed conformational change. Our observation that over half of the peptides (13 of 21) display changes in H/D exchange upon cofactor binding is in sharp contrast to the H/D exchange study of the NADH-dependent *E. coli* dihydrodipicolinate reductase (DHDR) (*60*). In that study, only 2 of 21 overlapping peptides displayed significant changes upon cofactor binding, indicating relatively small conformational and dynamic changes caused by cofactor binding for DHDR in comparison with htADH. These results suggest that the regions removed from the cofactor-binding pocket exhibit decreased dynamic mobility when the htADH enzyme adopts the closed-form structure.

It is interesting to note that a large region of the substrate-binding domain that consists of peptides 1−4, 7, and 9 does not show any noticeable changes upon cofactor binding in H/D exchange. An examination of the time-course plots of these peptides reveals that the exchange reaches equilibrium within the first 20 min and is dominated by fast kinetic components (see data in the Supporting Information). The lack of slow-exchanging hydrogens and a low level of deuteration indicate that this region is less flexible than other parts of the enzyme, as will be discussed in detail elsewhere (*27*). This region was also found to undergo a temperature-dependent transition to attain a more flexible state at elevated temperatures (*27*).

Factors Responsible for Thermophilic Behavior. Comparison of thermophilic htADH with its nearest available structural homolog, mesophilic EcADH, suggests structural motifs that are responsible for the thermophilic behavior. Several studies (*5*, *8*, *61*, *62*) have identified a variety of factors, some or all of which have been shown to be beneficial for particular thermophilic proteins. Among them are the number and location of proline residues, salt bridges, and hydrogen bonds. Proline is thought to add rigidity to a polypeptide chain, making it less likely that a protein will unfold, especially if the residue occurs in a flexible loop joining two segments of secondary structure (*63*). A comparison of the primary structures of htADH and EcADH shows that the former has twice as many proline residues as the latter, 18 versus 9 per subunit. Only 6 of the proline residues are conserved. Of the 12 nonconserved residues, 5 appear to contribute to the thermophilic properties of htADH. The first of these, Pro^{242}, aligns with an alanine residue in EcADH. The $Pro^{242} \rightarrow$ Ala mutation has been shown to promote the thermostability of htADH, as reported by Fiorentino et al. (*62*). In that study, the htADH enzyme activity at 75 °C was measured as a function of the incubation time. Whereas the wild-type enzyme showed 30% deactivation after 45 min, the activity of the $Pro^{242} \rightarrow$ Ala mutant dropped 50% in 26 min. The remaining four prolines are found in a stretch of 10 residues that form the pattern PXXPXXPXXP. These residues span sequence numbers 50−59 and lie in a region of the coiled conformation between an α helix and a β strand (Figure 2).

A list of salt bridges for htADH was compiled and compared with that for EcADH. The number of salt bridges in both enzymes is roughly equal. There are about 23 salt bridges per subunit in htADH versus about 19 per subunit in EcADH. The mesophilic enzyme has a slight edge in the number of intersubunit salt bridges, 17 versus 16 for htADH. It appears that the salt bridge location, not merely the total number of salt bridges, may be an important factor in explaining the enhanced thermostability of htADH. In this regard, a salt bridge involving the residues Glu^7, Lys^{14}, and Lys^{16} is of particular interest because of its position and the fact that the interaction is not possible in EcADH. As Figure 8 shows, this surface salt bridge serves to tie together two β strands across a flexible loop. Further support for the idea that this bridge plays a role in thermal stabilization comes

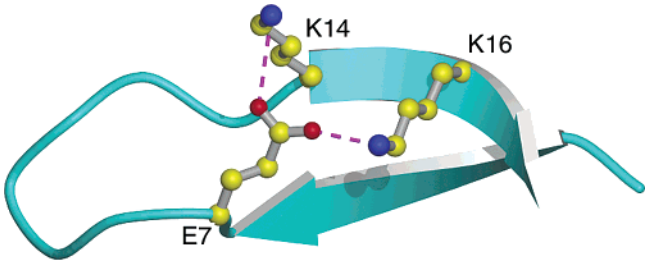

FIGURE 8: Salt bridge at the N terminus of htADH. The salt bridge ties together two β strands across a flexible loop. The salt bridge cannot occur in mesophilic EcADH, nor in ADH-T, a less thermophilic homologue of htADH. Hence, this interaction is likely to contribute to the thermal stability of htADH.

from a comparison of the protein sequence of htADH with that of ADH-T, a homologue from a less thermophilic strain of *B. stearothermophilus* (*64*). In the latter, the charged residue Lys^{14} has been replaced by glutamine, thereby eliminating this salt bridge.

The hydrogen-bond results do not appear to explain the enhanced thermostability of htADH over EcADH. There are more intra- and intersubunit hydrogen bonds in the mesophilic enzyme than in thermophilic htADH. On average, there are about 395 hydrogen bonds per subunit in EcADH, versus about 365 for htADH. There are 29 intersubunit hydrogen bonds in the tetramer of EcADH, more than twice as many as in htADH (12 in all).

We conclude that the enhanced thermostability of htADH compared to mesophilic EcADH depends primarily on the proline number and location, less critically on the strategic location of one or several salt bridges, and not at all on the number of hydrogen bonds. These results underscore observations reported by some authors (*65*−*67*) that no one factor is always responsible for the thermophilic behavior; that usually a combination of factors is involved; and finally that the combination of factors involved will be different for different proteins.

ACKNOWLEDGMENT

We thank Drs. Cannio and Bartolucci for the generous gift of htADH used for initial protein crystal screening, Dr. Eklund for providing the EcADH atomic coordinates prior to release from the PDB, and Dr. Ahn for assistance and resources to measure amide H/D exchange data.

SUPPORTING INFORMATION AVAILABLE

H/D exchange time-course plots for the peptides that do not show significant changes in deuteron incorporation upon cofactor binding shown for peptides 1−4, 7, 9, 10, and 13 (Supporting Figure 1). H/D exchange time courses for peptides that decrease in deuteron incorporation upon cofactor binding shown for peptides 5, 8, 11, 15−17, and 19−21 (Supporting Figure 2). This material is available free of charge via the Internet at http://pubs.acs.org.

REFERENCES

1. Fersht, A. R. (1998) in *Structure and Mechanism in Protein Science* (Julet, M. R., Ed.) pp 460−465, W. H. Freeman and Co., New York.
2. Jornvall, H., Persson, B., and Jeffery, J. (1987) Characteristics of alcohol/polyol dehydrogenases. The zinc-containing long-chain alcohol dehydrogenases, *Eur. J. Biochem. 167*, 195−201.
3. Karlsson, A., El-Ahmad, M., Johansson, K., Shafqat, J., Jornvall, H., Eklund, H., and Ramaswamy, S. (2003) Tetrameric NAD-dependent alcohol dehydrogenase, *Chem.-Biol. Interact. 143*−*144*, 239−245.
4. Korkhin, Y., Kalb (Gilboa), A. J., Peretz, M., Bogin, O., Burstein, Y., and Frolow, F. (1998) NADP-dependent bacterial alcohol dehydrogenases: Crystal structure, cofactor-binding and cofactor specificity of the ADHs of *Clostridium beijerinckii* and *Thermoanaerobacter brockii*, *J. Mol. Biol. 278*, 967−981.
5. Korkhin, Y., Kalb (Gilboa), A. J., Peretz, M., Bogin, O., Burstein, Y., and Frolow, F. (1999) Oligomeric integrity—the structural key to thermal stability in bacterial alcohol dehydrogenases, *Protein Sci. 8*, 1241−1249.
6. Li, C., Heatwole, J., Soelaiman, S., and Shoham, M. (1999) Crystal structure of a thermophilic alcohol dehydrogenase substrate complex suggests determinants of substrate specificity and thermostability, *Proteins: Struct., Funct., Genet. 37*, 619−627.
7. Esposito, L., Sica, F., Raia, C. A., Giordano, A., Rossi, M., Mazzarella, L., and Zagari, A. (2002) Crystal structure of the alcohol dehydrogenase from the hyperthermophilic archaeon *Sulfolobus solfataricus* at 1.85-Å resolution, *J. Mol. Biol. 318*, 463−477.
8. Bogin, O., Levin, I., Hacham, Y., Tel-Or, S., Peretz, M., Frolow, F., and Burstein, Y. (2002) Structural basis for the enhanced thermal stability of alcohol dehydrogenase mutants from the mesophilic bacterium *Clostridium beijerinckii*: Contribution of salt bridging, *Protein Sci. 11*, 2561−2574.
9. Adams, M. W., Perler, F. B., and Kelly, R. M. (1995) Extremozymes: Expanding the limits of biocatalysis, *Biotechnology 13*, 662−668.
10. Coolbear, T., Daniel, R. M., and Morgan, H. W. (1992) The enzymes from extreme thermophiles: Bacterial sources, thermostabilities and industrial relevance, *Adv. Biochem. Eng. Biotechnol. 45*, 57−98.
11. Kumar, S., Tsai, C. J., and Nussinov, R. (2000) Factors enhancing protein thermostability, *Protein Eng. 13*, 179−191.
12. Russell, R. J., and Taylor, G. L. (1995) Engineering thermostability: Lessons from thermophilic proteins, *Curr. Opin. Biotechnol. 6*, 370−374.
13. Kohen, A., and Klinman, J. P. (1998) Enzyme catalysis: Beyond classical paradigms, *Acc. Chem. Res. 31*, 397−404.
14. Cha, Y., Murray, C. J., and Klinman, J. P. (1989) Hydrogen tunneling in enzyme reactions, *Science 243*, 1325−1330.
15. Bahnson, B. J., Park, D. H., Kim, K., Plapp, B. V., and Klinman, J. P. (1993) Unmasking of hydrogen tunneling in the horse liver alcohol dehydrogenase reaction by site-directed mutagenesis, *Biochemistry 32*, 5503−5507.
16. Rubach, J. K., and Plapp, B. V. (2003) Amino acid residues in the nicotinamide binding site contribute to catalysis by horse liver alcohol dehydrogenase, *Biochemistry 42*, 2907−2915.
17. Bahnson, B. J., Colby, T. D., Chin, J. K., Goldstein, B. M., and Klinman, J. P. (1997) A link between protein structure and enzyme catalyzed hydrogen tunneling, *Proc. Natl. Acad. Sci. U.S.A. 94*, 12797−12802.
18. Billeter, S. R., Webb, S. P., Agarwal, P. K., Iordanov, T., and Hammes-Schiffer, S. (2001) Hydride transfer in liver alcohol dehydrogenase: Quantum dynamics, kinetic isotope effects, and role of enzyme motion, *J. Am. Chem. Soc. 123*, 11262−11272.
19. Kohen, A., and Jensen, J. H. (2002) Boundary conditions for the Swain-Schaad relationship as a criterion for hydrogen tunneling, *J. Am. Chem. Soc. 124*, 3858−3864.
20. Luo, J., and Bruice, T. C. (2001) Dynamic structures of horse liver alcohol dehydrogenase (HLADH): Results of molecular dynamics simulations of HLADH-NAD(+)-PhCH(2)OH, HLADH-NAD(+)-PhCH(2)O(−), and HLADH-NADH-PhCHO, *J. Am. Chem. Soc. 123*, 11952−11959.
21. Truhlar, D. G., Gao, J., Alhambra, C., Garcia-Viloca, M., Corchado, J., Sanchez, M. L., and Villa, J. (2002) The incorporation of quantum effects in enzyme kinetics modeling, *Acc. Chem. Res. 35*, 341−349.
22. Hammes-Schiffer, S. (2002) Impact of enzyme motion on activity, *Biochemistry 41*, 13335−13343.
23. Kohen, A., Cannio, R., Bartolucci, S., and Klinman, J. P. (1999) Enzyme dynamics and hydrogen tunnelling in a thermophilic alcohol dehydrogenase, *Nature 399*, 496−499.
24. Kohen, A., and Klinman, J. P. (2000) Protein flexibility correlates with degree of hydrogen tunneling in thermophilic and mesophilic alcohol dehydrogenases, *J. Am. Chem. Soc. 122*, 10738−10739.

25. Cannio, R., Rossi, M., and Bartolucci, S. (1994) A few amino acid substitutions are responsible for the higher thermostability of a novel NAD(+)-dependent bacillus alcohol dehydrogenase, *Eur. J. Biochem. 222*, 345−352.
26. Guagliardi, A., Martino, M., Iaccarino, I., De Rosa, M., Rossi, M., and Bartolucci, S. (1996) Purification and characterization of the alcohol dehydrogenase from a novel strain of *Bacillus stearothermophilus* growing at 70 °C, *Int. J. Biochem. Cell Biol. 28*, 239−246.
27. Liang, Z. X., Lee, T., Resing, K. A., Ahn, N. G., and Klinman, J. P. (2004) Thermal activated protein mobility and its correlation with catalysis in thermophilic alcohol dehydrogenase, submitted.
28. Otwinowski, Z., and Minor, W. (1997) Processing of X-ray diffraction data collected in oscillation mode, *Methods Enzymol. 276*, 307−326.
29. Navaza, J. (1994) Amore: An automated package for molecular replacement, *Acta Crystallogr., Sect. A 50*, 157−163.
30. *CCP4* (1994) The CCP4 suite: Programs for protein crystallography, *Acta Crystallogr., Sect. D. 50*, 760−763.
31. Brunger, A. T., Adams, P. D., Clore, G. M., DeLano, W. L., Gros, P., Grosse-Kunstleve, R. W., Jiang, J. S., Kuszewski, J., Nilges, M., Pannu, N. S., Read, R. J., Rice, L. M., Simonson, T., and Warren, G. L. (1998) Crystallography and NMR system: A new software suite for macromolecular structure determination, *Acta Crystallogr., Sect. D 54*, 905−921.
32. Cowtan, K. D., and Zhang, K. Y. (1999) Density modification for macromolecular phase improvement, *Prog. Biophys. Mol. Biol. 72*, 245−270.
33. Bricogne, G. (1974) Geometric sources of redundancy in intensity data and their use for phase determination, *Acta Crystallogr., Sect. A 30*, 395−405.
34. Zhang, K. Y., and Main, P. (1990) Histogram matching as a new density modification technique for phase refinement and extension of protein molecules, *Acta Crystallogr., Sect. A 46*, 41−46.
35. Wang, B. C. (1985) Resolution of phase ambiguity in macromolecular crystallography, *Methods Enzymol. 115*, 90−112.
36. Cowtan, K., and Main, P. (1998) Miscellaneous algorithms for density modification, *Acta Crystallogr., Sect. D 54*, 487−493.
37. Jones, T. A., Zou, J. Y., Cowan, S. W., and Kjeldgaard, M. (1991) Improved methods for binding protein models in electron density maps and the location of errors in these models, *Acta Crystallogr., Sect. A 47*, 110−119.
38. Russell, R. B., and Barton, G. J. (1992) Multiple protein sequence alignment from tertiary structure comparison: Assignment of global and residue confidence levels, *Proteins: Struct., Funct., Genet. 14*, 309−323.
39. Berman, H. M., Westbrook, J., Feng, Z., Gilliland, G., Bhat, T. N., Weissig, H., Shindyalov, I. N., and Bourne, P. E. (2000) The Protein Data Bank, *Nucleic Acids Res. 28*, 235−242.
40. Banfield, M. J., Salvucci, M. E., Baker, E. N., and Smith, C. A. (2001) Crystal structure of the NADP(H)-dependent ketose reductase from *Bemisia argentifolii* at 2.3-Å resolution, *J. Mol. Biol. 306*, 239−250.
41. Thompson, J. D., Higgins, D. G., and Gibson, T. J. (1994) Clustal W: Improving the sensitivity of progressive multiple sequence alignment through sequence weighting, position-specific gap penalties and weight matrix choice, *Nucleic Acids Res. 22*, 4673−4680.
42. Brunger, A. T. (1992) The free *R* value: A novel statistical quantity for assessing the accuracy of crystal structures, *Nature 355*, 472−474.
43. Jones, T. A. (1992) in *CCP4 Study Weekend* (Dodson, E. J., Gover, S., and Wolf, W., Eds.) pp 91−105, CLRC Daresbury Laboratory, Cheshire, U.K.
44. Kleywegt, G. J., and Read, R. J. (1997) Not your average density, *Structure 5*, 1557−1569.
45. Colby, T. D., Bahnson, B. J., Chin, J. K., Klinman, J. P., and Goldstein, B. M. (1998) Active site modifications in a double mutant of liver alcohol dehydrogenase: Structural studies of two enzyme−ligand complexes, *Biochemistry 37*, 9295−9304.
46. Kleywegt, G. J., and Jones, T. A. (1997) Model building and refinement practice, *Methods Enzymol. 277*, 208−230.
47. Barton, G. J. (1993) Alscript: A tool to format multiple sequence alignments, *Protein Eng. 6*, 37−40.
48. Kabsch, W., and Sander, C. (1983) Dictionary of protein secondary structure: Pattern recognition of hydrogen-bonded and geometrical features, *Biopolymers 22*, 2577−2637.
49. Kabsch, W. (1976) A solution for the best rotation to relate two sets of vectors, *Acta Crystallogr., Sect. A 32*, 922−923.
50. Kraulis, P. J. (1991) Molscript: A program to produce both detailed and schematic plots of protein structures, *J. Appl. Crystallogr. 24*, 946−950.
51. Laskowski, R. A., MacArthur, M. W., Moss, D. M., and Thornton, J. M. (1993) PROCHECK, *J. Appl. Crystallogr. 26*, 283.
52. Vaguine, A. A., Richelle, J., and Wodak, S. J. (1999) SFCHECK: A unified set of procedures for evaluating the quality of macromolecular structure-factor data and their agreement with the atomic model, *Acta Crystallogr., Sect. D 55*, 191−205.
53. Resing, K. A., Mansour, S. J., Hermann, A. S., Johnson, R. S., Candia, J. M., Fukasawa, K., Vande Woude, G. F., and Ahn, N. G. (1995) Determination of v-mos-catalyzed phosphorylation sites and autophosphorylation sites on map kinase kinase by ESI/MS, *Biochemistry 34*, 2610−2620.
54. Eklund, H., Nordstrom, B., Zeppezauer, E., Soderlund, G., Ohlsson, I., Boiwe, T., Soderberg, B., Tapia, O., Branden, C., and Akeson, A. (1976) Three-dimensional structure of horse liver alcohol dehydrogenase at 2.4-Å resolution, *J. Mol. Biol. 102*, 27−59.
55. Al-Karadaghi, S., Cedergren-Zeppezauer, E. S., Hoevmoller, S., Petratos, K., Terry, H., and Wilson, K. S. (1994) Refined crystal structure of liver alcohol dehydrogenase-NADH complex at 1.8-Å resolution, *Acta Crystallogr., Sect. D 50*, 793−807.
56. Eklund, H., Plapp, B. V., Samama, J. P., and Branden, C. I. (1982) Binding of substrate in a ternary complex of horse liver alcohol dehydrogenase, *J. Biol. Chem. 257*, 14349−14358.
57. Vieille, C., and Zeikus, G. J. (2001) Hyperthermophilic enzymes: Sources, uses, and molecular mechanisms for thermostability, *Microbiol. Mol. Biol. Rev. 65*, 1−43.
58. Zavodszky, P., Kardos, J., Svingor, and Petsko, G. A. (1998) Adjustment of conformational flexibility is a key event in the thermal adaptation of proteins, *Proc. Natl. Acad. Sci. U.S.A. 95*, 7406−7411.
59. Colonna-Cesari, F., Perahia, D., Karplus, M., Eklund, H., Branden, C. I., and Tapia, O. (1986) Interdomain motion in liver alcohol dehydrogenase. Structural and energetic analysis of the hinge-bending mode, *J. Biol. Chem. 261*, 15273−15280.
60. Wang, F., Blanchard, J. S., and Tang, X. J. (1997) Hydrogen exchange/electrospray ionization mass spectrometry studies of substrate and inhibitor binding and conformational changes of *Escherichia coli* dihydrodipicolinate reductase, *Biochemistry 36*, 3755−3759.
61. Wallon, G., Kryger, G., Lovett, S. T., Oshima, T., Ringe, D., and Petsko, G. A. (1997) Crystal structures of *Escherichia coli* and *Salmonella typhimurium* 3-isopropylmalate dehydrogenase and comparison with their thermophilic counterpart from *Thermus thermophilus*, *J. Mol. Biol. 266*, 1016−1031.
62. Fiorentino, G., Cannio, R., Rossi, M., and Bartolucci, S. (1998) Decreasing the stability and changing the substrate specificity of the *Bacillus stearothermophilus* alcohol dehydrogenase by single amino acid replacements, *Protein Eng. 11*, 925−930.
63. Watanabe, K., Masuda, T., Ohashi, H., Mihara, H., and Suzuki, Y. (1994) Multiple proline substitutions cumulatively thermostabilize *Bacillus cereus* atcc7064 oligo-1,6 glucosidase. Irrefragable proof supporting the proline rule, *Eur. J. Biochem. 226*, 277−283.
64. Sakoda, H., and Imanaka, T. (1992) Cloning and sequencing of the gene coding for alcohol dehydrogenase of *Bacillus stearothermophilus* and rational shift of the optimum pH, *J. Bacteriol. 174*, 1397−1402.
65. Korndorfer, I., Steipe, B., Huber, R., Tomschy, A., and Jaenicke, R. (1995) The crystal structure of holo-glyceraldehyde-3-phosphate dehydrogenase from the hyperthermophilic bacterium *Thermotoga maritima* at 2.5-Å resolution, *J. Mol. Biol. 246*, 511−521.
66. Russell, R. J., Hough, D. W., Danson, M. J., and Taylor, G. L. (1994) The crystal structure of citrate synthase from the thermophilic archaeon, *Thermoplasma acidophilum*, *Structure 2*, 1157−1167.
67. Fujinaga, M., Berthet-Colominas, C., Yaremchuk, A. D., Tukalo, M. A., and Cusack, S. (1993) Refined crystal structure of the seryltrna synthetase from *Thermus thermophilus* at 2.5-Å resolution, *J. Mol. Biol. 234*, 222−233.
68. Luzatti, P. V. (1952) Traitement statistique des erreurs dans la determination des structures cristallines, *Acta Crystallogr. 5*, 802−810.
69. Read, R. J. (1986) Improved Fourier coefficients for maps using phases from partial structures with errors, *Acta Crystallogr., Sect. A 42*, 140−149.

BI049736P